Influence of synthesis method on molybdenum carbide crystal structure and catalytic performance in stearic acid hydrodeoxygenation

Luana Souza Macedo[a,b], Ricardo R. Oliveira Jr.[c], Tomas van Haasterecht[b], Victor Teixeira da Silva[a], Harry Bitter[b,*]

[a] *Universidade Federal do Rio de Janeiro, NUCAT – Programa de Engenharia Química –COPPE, P.O. Box 68502, 21941-914, RJ, Rio de Janeiro, Brazil*
[b] *Wageningen University, Biobased Chemistry and Technology, P.O. Box 17, 6700 AA Wageningen, The Netherlands*
[c] *Universidade Federal do Rio de Janeiro, Departamento de Físico-Química, Instituto de Química, Cidade Universitária, CT, Bloco A, Rio de Janeiro, CEP 21941-909, Brazil*

ABSTRACT

The role of the synthesis method of molybdenum carbide nanoparticle catalysts supported on carbon nanofibers on crystal structure and on catalytic performance in hydrodeoxygenation of stearic acid was investigated. We obtained the cubic phase of molybdenum carbide (α-MoC$_{1-x}$) by impregnating carbon nanofibers with a solution of $(NH_4)_2MoO_4$, then exposing them to 20% CH_4/H_2 at 650 °C for 2 h. When increasing the Mo loading from 7.5 wt% to 20 wt% or using the carbothermal reduction method, i.e. using carbon from the support to reduce the $(NH_4)_2MoO_4$ precursor at 800 °C for 6 h, the hexagonal phase (β-Mo$_2$C) resulted.

Experiments with stearic acid hydrodeoxygenation showed that both phases (7.5 wt% Mo) displayed similar intrinsic activities. However, α-MoC$_{1-x}$/CNF reached 80% stearic acid conversion after 240 min while the β-Mo$_2$C/CNF catalyst attained the same conversion after 360 min. CO chemisorption results showed that α-MoC$_{1-x}$/CNF and β-Mo$_2$C/CNF have a similar number of potential active sites (66 and 56 μmol g^{-1}, respectively). We attribute the difference in catalytic performance between α-MoC$_{1-x}$/CNF and β-Mo$_2$C/CNF to differences in the catalyst's crystal structure, more specifically, the associated site density. The face-centered cubic α-MoC$_{1-x}$/CNF has a lower site density (0.1096 Mo atoms Å^{-2}) than the hexagonal close-packed β-Mo$_2$C/CNF (0.1402 Mo atoms Å^{-2}), making the Mo atoms at the surface of the α-MoC$_{1-x}$ phase more accessible for large reactant molecules such as stearic acid thus allowing its convertion in shorter times.

1. Introduction

Noble metals are widely used in catalysis, amongst others, for reactions such as (de)hydrogenation, hydrogenolysis and Fischer-Tropsch synthesis [1]. However, noble metals are scarce, hence expensive, which makes it desirable to find more abundant alternatives.

Since the seminal work of Levy and Boudart [2], it has become clear that transition metal carbides are efficient catalysts for reactions that involve the transfer of hydrogen, such as ammonia synthesis, hydrogenation, hydrogenolysis, isomerization, methanation and hydroprocessing [3]. Lately, W and C carbides have gained interest as active catalysts for biomass conversion, e.g. in the conversion of lignin, hemicellulose and cellulose [4–7] or in the conversion of triglycerides [8,9]. Recently, we showed that Mo and W carbide catalysts are also active for biomass-related conversions such as deoxygenation of stearic and oleic acids [10–12] and gamma-valerolactone production via

levulinic acid hydrogenation [13].

For a number of reactions, transition metal carbides display similar or even better catalytic performance than noble metal catalysts. For example, Dhandapani et al. [14] found that Mo$_2$C is more active than Pt/γ-Al$_2$O$_3$ for cumene hydrogenation and Li et al. [15], Claridge et al. [16] and Choi et al. [17] reported that the catalytic activity of the transition metal carbides Ni-W$_2$C, Mo$_2$C and W$_2$C can compete with that of noble metal catalysts in wood lignin degradation, conversion of methane to synthesis gas and benzene hydrogenation, respectively.

A typical method to synthesize transition metal carbides, especially molybdenum and tungsten carbides, is the temperature-programmed reaction (TPR) method [3]. First, a support is impregnated with a soluble oxidic precursor and then the sample is calcined forming a supported oxide. In the next step, the oxide is heated in a carbon-containing atmosphere such as methane or butane [10,18], which converts the oxide into the carbide. Depending on the carburizing gas

composition during TPR, different crystallographic structures of the final catalyst result. For example, Xiao et al. [18] produced the face-centered-cubic form of molybdenum carbide after synthesis with 5% C_4H_{10} and 95% H_2 as carburizing gas, while Sousa et al. [10] created hexagonal molybdenum carbide after synthesis with 20% CH_4 and 80% H_2 as carburizing gas, both at 650 °C for 2 h and using supported molybdenum trioxide as precursor.

Another method used to synthesize transition metal carbides is carbothermal reduction [19]. A carbon-based support impregnated with an oxidic precursor is heated in a carbon-free atmosphere. The carbide forms by reaction of the oxide with carbon from the support [11,12,19–23]. This method has the advantage of avoiding carbon deposition on the catalyst surface, which commonly occurs with the TPR method due to methane (or hydrocarbon) decomposition [3].

Despite the increasing number of reports that show the potential of transition metal carbides as catalysts for various reactions, they are not widely used in commercial applications. Here, we try to understand the property-performance relationship for the carbides to advance that field [3,24–26].

Controlling the crystal structure of the carbides is important because it can have a significant influence on catalytic performance, although there are cases in which crystal structure does not influence catalytic performance. For example, α-MoC_{1-x} and β-Mo_2C phases displayed a similar catalytic activity for isopropanol dehydration at 140 °C in an inert He/Ar atmosphere as well as in 13 kPa O_2 [27]. On the other hand, for dehydrogenation of benzyl alcohol [28], steam reforming of methanol [29] and hydrogenation of toluene [30], β-Mo_2C was more active than α-MoC_{1-x} while α-MoC_{1-x} was more active than β-Mo_2C for CO hydrogenation to produce methane [31].

Various ways exist to control the crystal structure of the carbide, such as by temperature, nature of the oxidic precursor, percentage of weight-loading and carburizing atmosphere composition [27–29,31–34]. For example, the combination of a low temperature (250–400 °C) with an H_2 atmosphere seems to favor the formation of a molybdenum bronze phase (H_xMoO_3, [35]) which is then topotactically transformed into the cubic molybdenum carbide phase, even in the case of a low carbon content (supplied C/Mo molar ratio = 0.6) [30]. The cubic phase also forms in the absence of H_2 at a high temperature (800 °C) and a supplied C/Mo ratio of 6.3 [30]. However, using a supplied C/Mo ratio of 2, no H_2 and a high temperature (800 °C) yields the hexagonal phase form [30]. Frank et al. [29] compared the TPR and carbothermal reduction methods for carbon-nanotube-supported molybdenum carbides and found that TPR of $(NH_4)_6Mo_7O_{24}.4H_2O$ in 20% CH_4/H_2 results in 2-nm crystallites of cubic α-MoC_{1-x} whereas TPR in pure H_2 and using the carbothermal method with He yields larger (8–10 nm) particles of hexagonal β-Mo_2C. Li et al. [28] showed that carburization of a bulk α-MoO_3 precursor in 20% CH_4/H_2 at 850 °C for 4 h results in the hexagonal β-Mo_2C phase, while α-MoC_{1-x} phase forms during TPR with 5% n-C_4H_{10}/H_2 at 700 °C for 4 h.

Though a consistent picture of the role of crystal structure on catalytic performance is still lacking, explanations have been put forward for the differences in the catalytic properties of these two molybdenum carbide forms, including differences in the reactant's adsorption energy [31] and differences in the (inadvertent) coverage of Mo atoms by carbon as occurs with the TPR method [28,30].

Comparisons of the catalytic performance of both forms in reactions involving lipid-based biomass, such as used in the production of olefins and paraffins, are still lacking. In this paper, we report on an investigation into the influence that the synthesis history of α-MoC_{1-x} or β-Mo_2C supported on carbon nanofibers has on their characteristics and performance as catalysts for the hydrodeoxygenation of stearic acid. We tested the catalysts under identical conditions to gain insight in the structure-performance relationship.

2. Experimental

2.1. Synthesis

Carbon nanofibers (CNF) were synthesized from a reduced 5 wt% Ni/SiO_2 catalyst (5 g) and a mixture of hydrogen (102 mL min^{-1}), nitrogen (450 mL min^{-1}) and carbon monoxide (266 mL min^{-1}) at 550 °C and 3.8 bar for 24 h, as previously reported [12]. Next, the CNF were refluxed in 400 mL 1 M KOH for 1 h to remove the SiO_2, followed by decanting and washing of the residue with 200 mL 1 M KOH. This treatment was repeated three times. After the final reflux, the material was washed with demi water. Subsequently, the solid was treated by refluxing it in 400 mL 65% HNO_3 for 1.5 h to remove exposed Ni and to add O_2-containing groups to the surface of the CNF. Finally, the CNF were washed with demi water to a neutral pH (measured with pH testing strips) of the washing water.

Supported oxides were prepared by impregnating 5 g of CNF four times with 7 mL of a 0.63 M solution of $(NH_4)_2MoO_4$ (Sigma-Aldrich, 99.98% trace metals basis) using incipient wetness impregnation. Between impregnations, the impregnated materials were dried in static air at 120 °C for 1 h. The pore volume of CNF is 0.43 mL g^{-1} (B.E.T analysis). This procedure resulted in a catalyst loading of 7.5 wt% Mo. For a Mo loading of 20 wt%, 5 g of CNF were impregnated ten times with in total 20 mL of a 1.86 M solution of $(NH_4)_2MoO_4$.

The supported oxides (0.4 g) were transformed to carbides in two different ways, namely via the TPR method and via the carbothermal reduction method. In the TPR method, the precursor was exposed to 20% CH_4/H_2 (CH_4 = 20 mL min^{-1} and H_2 = 80 mL min^{-1}). The temperature was increased from room temperature (20 °C) to 650 °C (β = 2.5 °C min^{-1}) and maintained at that temperature for 2 h. For carbothermal reduction, the precursor was heated from 20 °C to 800 °C (β = 5 °C min^{-1}) and kept at that temperature for 6 h under an argon flow of 100 mL min^{-1}.

2.2. Characterization

In-situ X-ray diffraction (XRD) was performed with a Rigaku DMax 2200 equipped with an Anton Paar XRK-900 reaction chamber, a Cu K_α tube and a graphite monochromator. Diffraction patterns were measured from $2\theta = 20°$ to $2\theta = 80°$ with a scan rate of 2° min^{-1}.

Samples were carburized in situ by using either 100 mL min^{-1} 20% CH_4/H_2 (TPR method) or argon (carbothermal reduction). The phase changes were followed by recording diffractograms at different temperatures. Between measurements, the sample was heated to the next temperature at 2.5 and 5 °C min^{-1} for TPR and carbothermal reduction, respectively.

The crystalline phase was identified with the aid of the Powder Diffraction File, a database of X-ray powder diffraction patterns maintained by the International Center for Diffraction Data (ICDD). This database is part of the JADE 5.0 software.

Nitrogen physisorption was used to assess the textural properties of the samples. Nitrogen adsorption/desorption isotherms were recorded at liquid nitrogen temperature using a Micromeritics TriStar. Before measurement the samples were pretreated in a vacuum at 400 °C for 20 h.

To assess the number of (potentially) active sites, we used CO chemisorption. Supported oxides (0.1 g) were first pretreated with 50 mL min^{-1} He at 500 °C for 30 min. Then the temperature was lowered and the catalyst was activated via carburization (20 mL min^{-1} CH_4 and 80 mL min^{-1} H_2) or carbothermal reduction (100 mL min^{-1} He). Samples were cooled down to 30 °C and flushed with He (50 mL min^{-1}) for 30 min. CO-pulse chemisorption measurements were performed using a custom-made multipurpose instrument by pulsing calibrated volumes of a 20% (v/v) CO/He gas mixture over the catalyst. Mass spectrometry (Prisma, equipped with a Pfeiffer vacuum pump, model D-35614) was used to assess the CO uptake.

As shown in the Suplementary Information, we calculated turnover frequency (TOF) with the equation: $TOF(s^{-1}) = \frac{-r_A}{CO_{uptake}}$, $-r_A = \frac{N_{A0} \times dx_A/dt}{W}$, in which $-r_A$ is the initial reaction rate (mmol g^{-1} s^{-1}), N_{A0} is the initial amount of stearic acid (mmol), dx_A/dt is the derivative of stearic acid conversion at time zero (s^{-1}) and W is the amount of catalyst (g).

Temperature-programmed desorption (TPD) of CO was carried out after CO chemisorption. Samples were heated from 20 °C to 1000 °C under He flow (100 mL min^{-1} and β = 15 °C min^{-1}) and the signal of ion $m/z = 28$ was followed in the mass spectrometer.

Transmission electron microscopy (TEM) was used to analyze particle size and size distribution. We mounted the samples on a 200-mesh copper grid covered with a pure carbon film. Samples were dusted onto the surface of the grid and any excess was removed. Analysis was performed in a JEOL JEM2100 transmission electron microscope operated at 200 kV. We took images (4k x 4k) with a Gatan US4000 camera. We calculated average particle sizes with ImageJ software, on the basis of 250–350 particles.

2.3. Hydrodeoxygenation

Hydrodeoxygenation (HDO) reactions were performed in a 100-mL stainless steel Parr autoclave reactor (4590 Micro Reactor). The reactor was filled with 2 g of stearic acid (Sigma-Aldrich, ≥ 95%, FCC, FG), 1 g of tetradecane (internal standard, Aldrich Chemistry, ≥ 99%), 0.25 g of catalyst (they were transferred directly from the synthesis equipment to the reactor by exposing them shortly to air) and 50 mL of dodecane as solvent (Sigma-Aldrich, ReagentPlus ®, ≥ 99%). After purging with argon, stirring at 800 rpm was started and the reactor was heated to 350 °C. At this temperature, the total pressure was 10 bar. Subsequently, 30 bar H$_2$ was added to the system, resulting in a final pressure of 40 bar. Samples of 1 mL were taken during the 6-hour reaction after 0, 20, 40, 60, 120, 180, 240, 300 and 360 min.

Gas chromatography (GC) was used to analyze the reaction mixture (Shimadzu 2014, equipped with CP-FFAP column and photoionization detector). We used the following column temperature program: 50 °C for 1 min, heating to 170 °C (β = 7 °C min^{-1}), dwell time 1 min, ramp to 240 °C (β = 4 °C min^{-1}), dwell time 15 min. Prior to GC, we diluted the samples in CH$_3$Cl:MeOH (2:1 v/v). Trimethylsulphonium hydroxide (Sigma-Aldrich, ~ 0.25 M in methanol, for GC derivatization) was added to methylate free acids. The injected volume was 1 μL for all analyses.

3. Results and discussion

3.1. Synthesis

Fig. 1 displays the in-situ XRD diffractograms of an impregnated, supported 7.5 wt% Mo precursor during its transformation via the carbothermal reduction method. The relevant phases are the MoO$_2$ phase (indicated by the purple triangles) and the hexagonal β-Mo$_2$C phase (indicated by the red squares).

The diffractions at about 2θ = 28 and 2θ = 43° represent the (002) and (101) reflections of the CNF [36]. Up to 500 °C, no other reflections were visible, indicating that the impregnated oxidic phase either consisted of very small crystallites or was amorphous. In the temperature range of 500–700 °C, diffraction lines representing MoO$_2$ (PDF# 32-0671) became visible. At 800 °C, these reflections started to disappear again and the reflection representing β-Mo$_2$C (PDF#35-0708) appeared. The β-Mo$_2$C reflections sharpened when the catalyst was held at 800 °C for a prolonged time (up to 6 h). Please note that the intensity of the CNF peak decreased during the experiment. We tentatively attribute this to the absorption of the X-rays by the large molybdenum carbide particles formed during the synthesis, as has previously been shown for Mo/ZSM-5 [37].
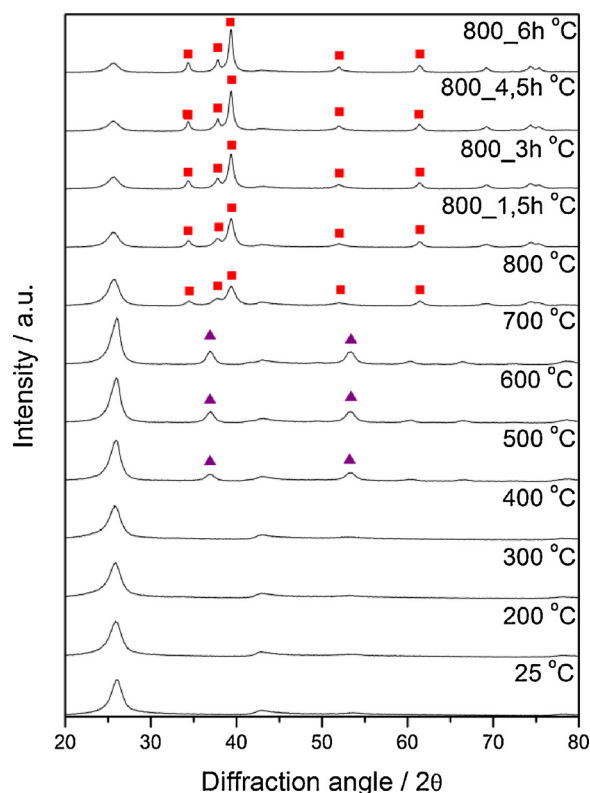

Fig. 1. In-situ XRD diffractogram for 7.5 wt% Mo$_2$C/CNF synthesized via carbothermal reduction with argon (with ■ indicating hexagonal β-Mo$_2$C and ▲ MoO$_2$).

We obtained the diffractograms shown in Fig. 1 during transformation of the molybdenum oxide precursor into carbide. Since it took around 40 min for each XRD diffractogram to be taken, we could not rule out that sintering occurred. Therefore, to calculate the particle size, we took a new sample of molybdenum oxide precursor and synthesized the catalyst in situ via the carbothermal reduction method, passivated it for 24 h in 0.5% O$_2$/He, and performed XRD at the end of synthesis process (Fig. S1). Based on the line broadening of the 39.39° peak and using the Scherrer equation, we calculated the average carbide crystallite size as 13 nm after 6 h at 800 °C.

Fig. 2 displays the diffractograms of an impregnated, supported 7.5 wt% Mo precursor during its transformation when using the TPR method with 20% CH$_4$/H$_2$ as carburization gas mixture. The blue rhombi indicate the reflections representing the cubic α-MoC$_{1-x}$ phase.

The signals at about 2θ = 28 and 2θ = 43° represent the (002) and (101) reflections of the CNF [36]. Up to 500 °C, no other reflections were visible, which indicates that the impregnated oxidic phase either consisted of very small crystallites or was amorphous. In the temperature range of 500 °C–650 °C, diffraction lines (blue rhombus) representing the α-MoC$_{1-x}$ phase (PDF#15-0457) became visible. The diffraction lines of α-MoC$_{1-x}$ were too broad and their intensity was too low to allow calculation of the crystallite size. In fact, Sebakhy et al. [38] found similar results when synthesized cubic and hexagonal molybdenum carbides. The bulk β-Mo$_2$C (hexagonal) presented a defined XRD diffractograms with narrow signals and average particle size of 37 nm and, on the other hand, the bulk α-MoC$_{1-x}$ (cubic) presented broad signal on the XRD diffractogram and an average particle size of 2 nm.

To summarize, synthesis via carbothermal reduction resulted in the hexagonal β-Mo$_2$C phase while use of the TPR method in 20% CH$_4$/H$_2$ produced cubic α-MoC$_{1-x}$.

Previous research has shown that the α-MoC$_{1-x}$ phase forms at higher C/Mo ratios and the β-Mo$_2$C phase at lower C/Mo ratios [28,30].
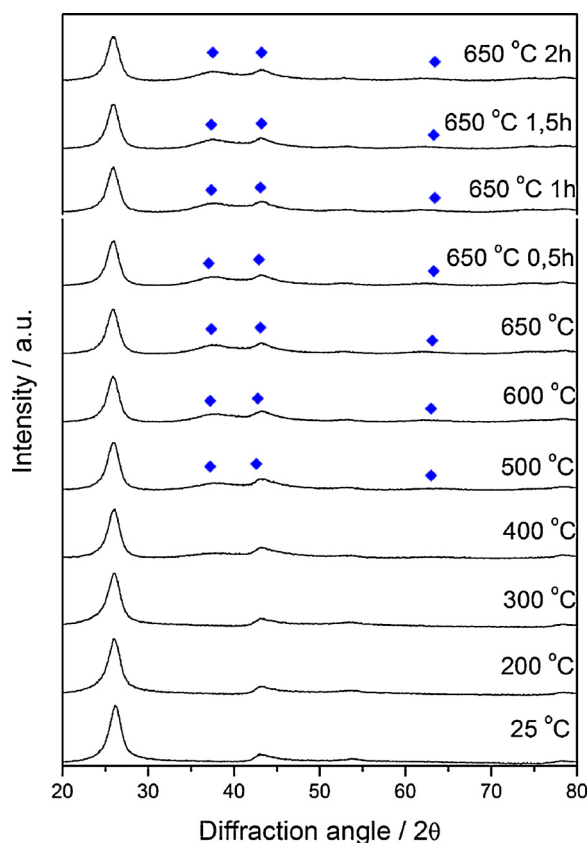
Fig. 2. In-situ XRD diffractogram for 7.5 wt% Mo_2C/CNF synthesized via carburization with 20% CH_4/H_2 gas mixture (◆ indicates cubic $\alpha-MoC_{1-x}$).

Table 1
Textural properties of CNF, $\alpha-MoC_{1-x}/CNF$ and $\beta-Mo_2C/CNF$ (7.5 wt% Mo).

	Surface Area $(m^2\,g^{-1})$	Micropore Area $(m^2\,g^{-1})$	Micropore Volume $(cm^3\,g^{-1})$	Pore volume $(cm^3\,g^{-1})$	Pores average size (Å)
CNF	180	20	0.009	0.43	136
$\alpha-MoC_{1-x}/CNF$	140	2	0	0.31	100
$\beta-Mo_2C/CNF$	130	4	0.001	0.40	155

Therefore, we also prepared a 20 wt% Mo sample (C/Mo molar ratio = 746, see Supplementary Information) under the same synthesis conditions as for the 7.5 wt% Mo (C/Mo molar ratio = 1989). XRD patterns of 20 wt% Mo supported molybdenum carbide synthesized via TPR with 20% CH_4/H_2 at 650 °C for 2 h shows that using the lower C/Mo ratio resulted in $\beta-Mo_2C$ (Fig. S2), in line with what others have reported.

3.2. Characterization

From now on, we will only consider the 7.5 wt% Mo samples because we are interested in compare the $\alpha-MoC_{1-x}/CNF$ and $\beta-Mo_2C/CNF$ catalysts in a weight basis. Table 1 lists the textural properties of CNF, $\alpha-MoC_{1-x}/CNF$ and $\beta-Mo_2C/CNF$. The parent CNF had a surface area of 180 $m^2\,g^{-1}$, which is comparable to the values reported in the literature for CNF made via the same synthesis protocol [11,39]. Cubic $\alpha-MoC_{1-x}/CNF$ and hexagonal $\beta-Mo_2C/CNF$ showed a similar surface area, of 140 $m^2\,g^{-1}$ and 130 $m^2\,g^{-1}$, respectively, which is lower than that of the parent CNF. Since molybdenum carbide precursor (MoO_3) is non-porous [10], the lower surface area of the supported catalysts can be partially explained by loading of the support with the carbides. However, this cannot fully explain the decrease in surface area, since only 7.5 wt% Mo was loaded. This suggests that part of the pores of the support were blocked by the carbides. This idea is supported by the significant decrease (higher than the 7.5% from the added MoO_3) we found in the micropore area of the catalysts (from 20 $m^2\,g^{-1}$ to 2 and 4 $m^2\,g^{-1}$ for $\alpha-MoC_{1-x}/CNF$ and $\beta-Mo_2C/CNF$, respectively) and the micropore volume (from 0.009 $cm^3\,g^{-1}$ to 0 and 0.001 $cm^3\,g^{-1}$ for $\alpha-MoC_{1-x}/CNF$ and $\beta-Mo_2C/CNF$, respectively) relative to the pure CNF. We tentatively explain the smaller pore area of $\alpha-MoC_{1-x}/CNF$ by the presence of carbonaceous deposits on that sample formed due to methane decomposition. Since that sample was prepared by the TPR method, deposits could have formed from decomposition of the carbon source (CH_4) during synthesis [3].

Fig. 3 displays representative HR-TEM images of $\alpha-MoC_{1-x}/CNF$ and $\beta-Mo_2C/CNF$. Black spots indicate the presence of the carbide or partly oxidized carbide (indicated with the red arrows) and the dark grey area is the CNF. Fig. 4 presents histograms of the particle size distribution of the $\alpha-MoC_{1-x}/CNF$ and $\beta-Mo_2C/CNF$ catalysts. We found an average particle size of 2 nm (s = 1.4 nm) for the $\alpha-MoC_{1-x}/CNF$ and of 6 nm (s = 9 nm) for the $\beta-Mo_2C/CNF$. The latter sample has a bimodal distribution with a few very large particles, resulting in a large standard deviation. The smaller particle size node appears similar to that of $\alpha-MoC_{1-x}/CNF$ particles (Fig. 4A), what can implicate that the smaller
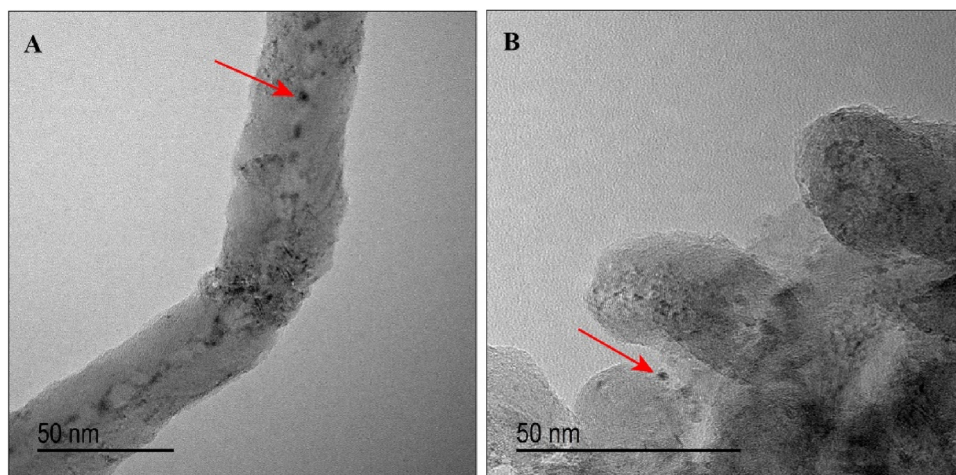

Fig. 3. HR-TEM images of A) $\alpha-MoC_{1-x}/CNF$ and B) $\beta-Mo_2C/CNF$.
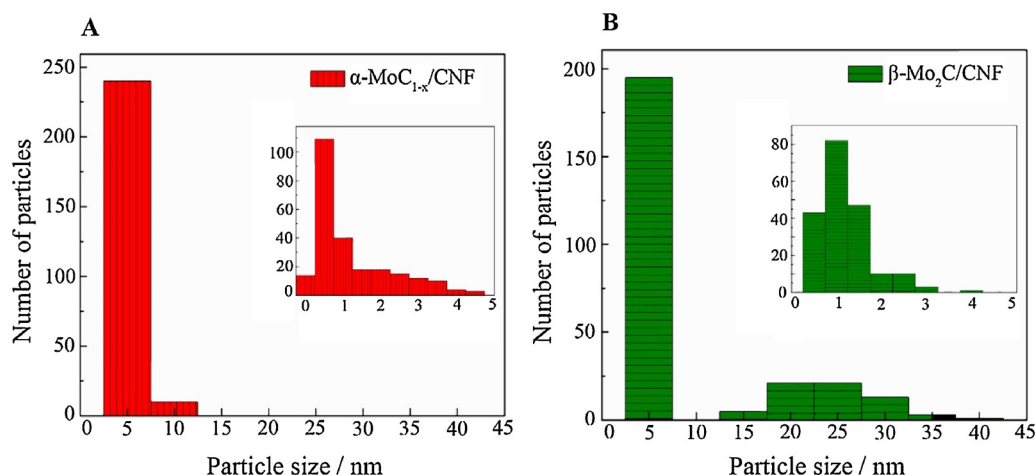
A

B

Fig. 4. Particle size distribution of A) α-MoC$_{1-x}$/CNF and B) β-Mo$_2$C/CNF. Secondary graphs represents a detail up to 5 nm.

Table 2
CO chemisorption uptake for CNF, α-MoC$_{1-x}$/CNF and β-Mo$_2$C/CNF.

	CO uptake (µmol g^{-1})
CNF	1
α-MoC$_{1-x}$/CNF	66 ± 3.3
β-Mo$_2$C/CNF	56 ± 2.8
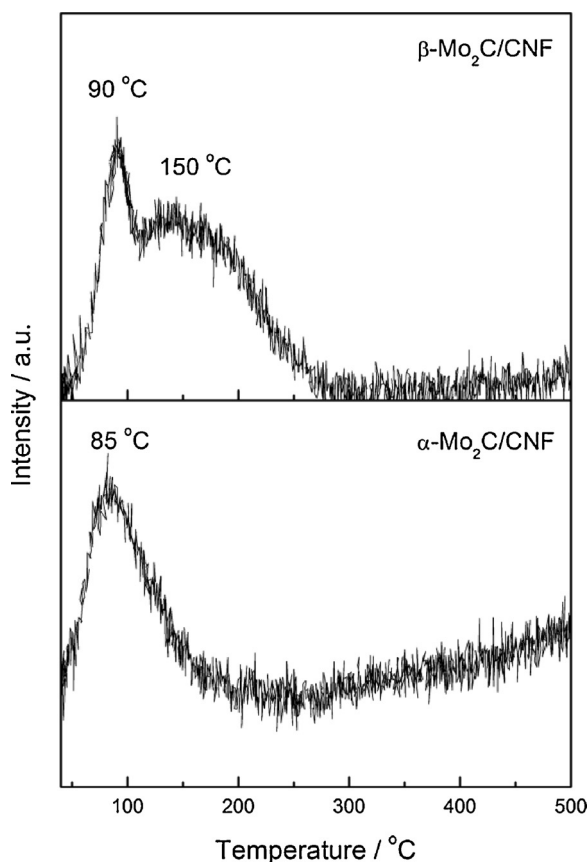
Fig. 5. Temperature-programmed desorption of CO for α-MoC$_{1-x}$/CNF and β-Mo$_2$C/CNF.

particles in Fig. 4B begin as α-MoC$_{1-x}$ and larger particles convert into the β-Mo$_2$C. XRD diffractograms in Fig. 2 show that the formation of α-MoC$_{1-x}$ phase is connected to the peaks at 2θ = 37.8° and 43°, but the
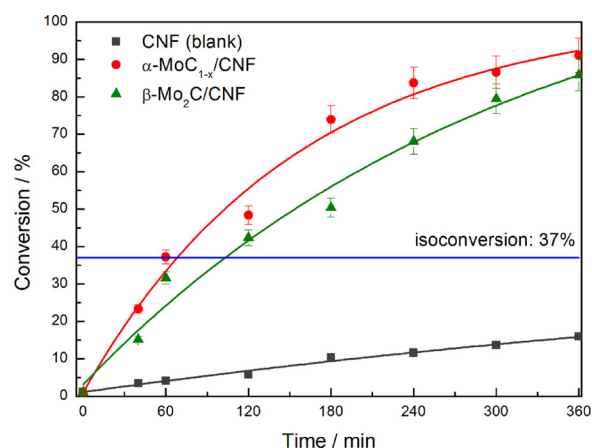

Fig. 6. Stearic acid conversion over α-MoC$_{1-x}$/CNF and β-Mo$_2$C/CNF (250 mg catalyst, 2 g stearic acid, 50 mL solvent, 30 bar H$_2$, T = 350 °C). The lines are added to guide the eyes.

peak at 2θ = 43° is also connected to the CNF support. Thus, we only can associate the formation of α-MoC$_{1-x}$ phase to the diffractogram peak at 2θ = 37.8°. Since we cannot clearly see a shoulder/peak at 2θ = 37.8° in Fig. 1 (β-Mo$_2$C/CNF), we cannot exclude that some α-MoC$_{1-x}$ is present in the β-Mo$_2$C/CNF catalyst. Note that the comparison of catalytic performance between α-MoC$_{1-x}$/CNF and β-Mo$_2$C/CNF catalysts will not be compromised even if some α-MoC$_{1-x}$ is present in the β-Mo$_2$C/CNF catalyst because the performance of the pure α-MoC$_{1-x}$ phase is obtained by α-MoC$_{1-x}$/CNF catalyst. Therefore, any difference in the performance of β-Mo$_2$C/CNF catalyst must be attributed to the β-Mo$_2$C phase.

To determine the number of potential active sites, pulse CO chemisorption was used. Table 2 shows the CO chemisorption uptakes of CNF, α-MoC$_{1-x}$/CNF and β-Mo$_2$C/CNF. CO chemisorption uptake by α-MoC$_{1-x}$/CNF (66 µmol g$_{cat}$$^{-1}$) was slightly higher than CO chemisorption uptake by β-Mo$_2$C/CNF (56 µmol g$_{cat}$$^{-1}$), meaning that α-MoC$_{1-x}$/CNF has more sites accessible for CO than β-Mo$_2$C/CNF. The CO chemisorption capacity of the CNF was negligible (1 µmol g$_{cat}$$^{-1}$).

In line with other studies [17,40–42], we used the CO chemisorption uptake to determine the number of potential active sites. However, this is not undisputed. For example, Clair et al. [43] argued that only 14% of the total number of surface Mo atoms is titrated via CO chemisorption over hexagonal molybdenum carbide (0001). For the sake of completeness and comparison, we therefore also report the particles size as calculated via TEM and XRD analysis (Table S1).

Though pulse chemisorption provides information on the number of available sites, it does not reveal anything about the nature of the sites
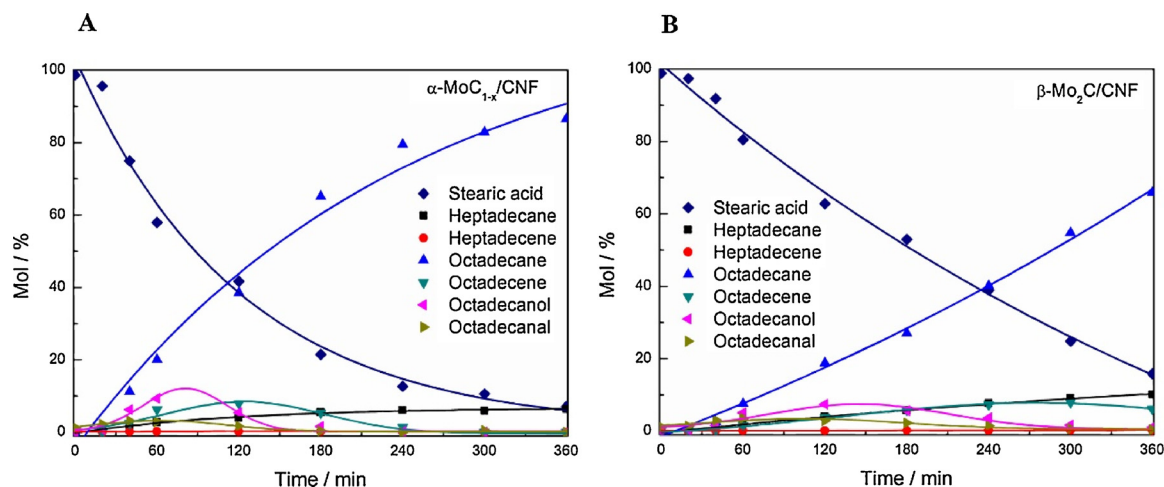
Fig. 7. Product concentration (%mol) over time for A) α-MoC$_{1-x}$/CNF and B) β-Mo$_2$C/CNF for stearic acid HDO (250 mg catalyst, 2 g stearic acid, 50 mL solvent, 30 bar H$_2$, T = 350 °C). The lines are added to guide the eyes.
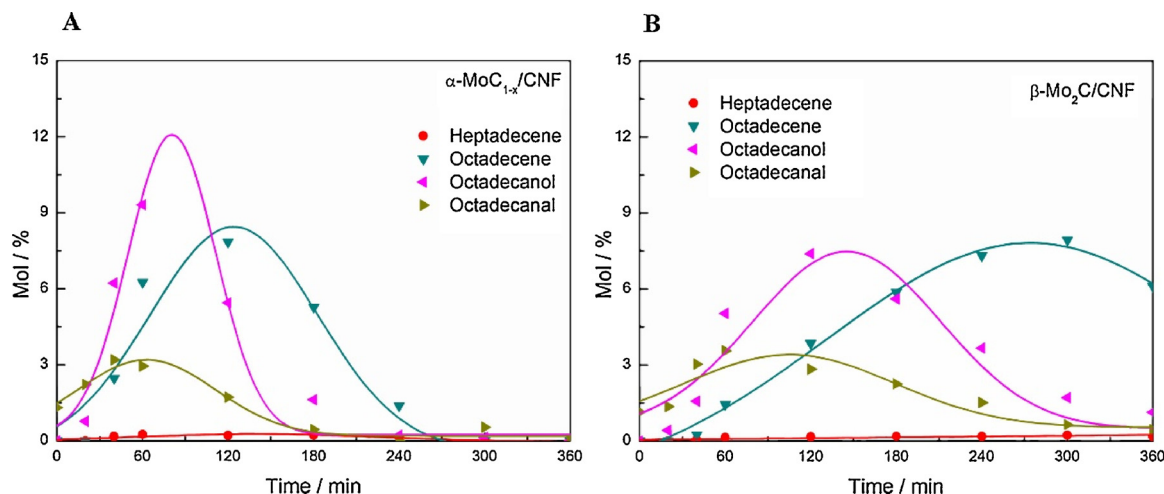

Fig. 8. Detail of intermediate product concentration (%mol) over time for A) α-MoC$_{1-x}$/CNF and B) β-Mo$_2$C/CNF during stearic acid HDO (250 mg catalyst, 2 g stearic acid, 50 mL solvent, 30 bar H$_2$, T = 350 °C). The lines are added to guide the eyes.
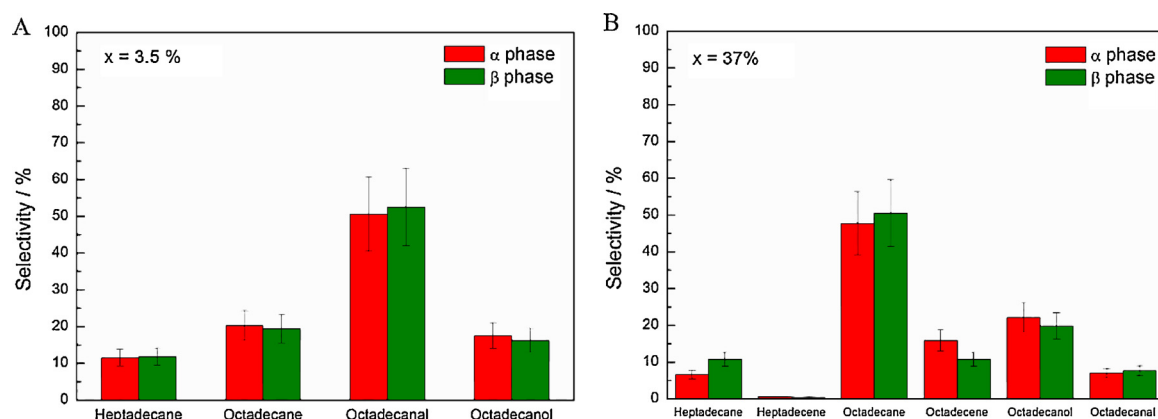

Fig. 9. Product distribution of α-MoC$_{1-x}$/CNF and β-Mo$_2$C/CNF catalysts for stearic acid HDO (250 mg catalyst, 2 g stearic acid, 50 mL solvent, 30 bar H$_2$, T = 350 °C) at isoconversion of A) 3.5% and B) 37%.

(CO binding strength). We assessed the latter by performing CO temperature-programmed desorption (TPD) after the chemisorption experiment. Fig. 5 displays the CO TPD trace for α-MoC$_{1-x}$/CNF and β-Mo$_2$C/CNF. α-MoC$_{1-x}$/CNF presented a defined CO desorption peak in the temperature region of 50 °C–200 °C with a maximum at 85 °C and β-

Mo$_2$C/CNF presented a clear CO desorption peak at 90 °C and a second peak at 150 °C. Frank et al. [29], Nagai et al. [44] and Shi et al. [45] have attributed these different binding strengths to CO bonds at the Mo sites (desorption at 85 °C–90 °C) and at the C sites (desorption at 150 °C).
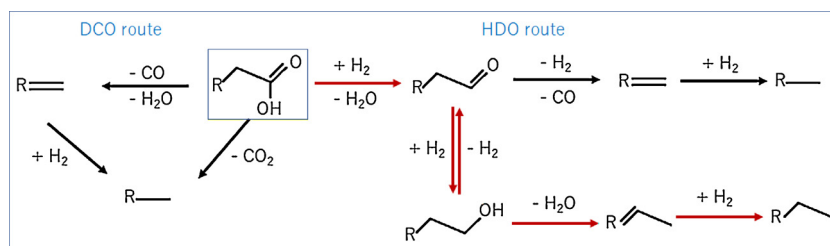
Fig. 10. Scheme of reaction pathways in deoxygenation of stearic acid, red arrow indicate the dominant pathway over Mo-carbides. (For interpretation of the references to colour in this figure legend, the reader is referred to the web version of this article.)

Table 3
Lattice parameters and site density of bulk cubic (fcc) α-MoC$_{1-x}$ and the hexagonal (hcp) β-Mo$_2$C based on literature data [47].

	Lattice parameters			Site density (Mo atoms Å^{-1})
	a/pm	b/pm	c/pm	
α-MoC$_{1-x}$	—	437.3[a]	—	0.1096
β-Mo$_2$C	—	582.7[a]	283.8[a]	0.1402

[a] Ref. [41].

3.3. Catalytic activity

Fig. 6 shows the catalytic activity (stearic acid conversion) of α-MoC$_{1-x}$/CNF and β-Mo$_2$C/CNF during 6 h of reaction. Since both catalysts contain the same amount of carbide, the conclusion is that on a weight basis, the catalyst containing the α-MoC$_{1-x}$ phase is more active than the catalyst with the β-Mo$_2$C phase. However, when the activity is normalized to the total number of binding sites (Table 2) as determined by CO uptake, the TOF is 3 s^{-1} for α-MoC$_{1-x}$ and 1s^{-1} for β-Mo$_2$C. This indicates that both catalysts have a similar intrinsic activity. We also carried out a reaction in which we used the pure CNF support. As Fig. 6 shows, the activity of CNF alone was an order of magnitude lower than that of the catalysts.

Fig. 7 depicts the product distribution of α-MoC$_{1-x}$/CNF (7 A) and β-Mo$_2$C/CNF (7B) for 360 min of reaction. Both catalysts yielded heptadecane, heptadecene, octadecane, octadecene, octadecanol and octadecanal as intermediates or final products, indicating that the reaction pathway is probably the same for both catalysts. However, the intermediate compounds were produced and consumed at different times.

To analyze the production and consumption of intermediate compounds over the α-MoC$_{1-x}$/CNF and β-Mo$_2$C/CNF catalysts, we looked at the evolution of heptadecene, octadecene, octadecanal and octadecanol over time (Fig. 8). Octadecanal and octadecanol were formed and consumed at different rates over the two catalysts. Over α-MoC$_{1-x}$/CNF, the intermediates were completely consumed after 240 min, while they were not fully consumed yet after 300 min over β-Mo$_2$C/CNF.

Moreover, octadecene reached a maximum concentration at 120 min over the α-MoC$_{1-x}$/CNF catalyst while that point was only reached after 300 min for β-Mo$_2$C/CNF. This confirms in greater detail that although the reaction pathway is the same and the same intermediates (heptadecene, octadecene, octadecanal and octadecanol) were present during stearic acid HDO over α-MoC$_{1-x}$/CNF and β-Mo$_2$C/CNF, they were produced and consumed at different times.

Fig. 9 presents the selectivities of both catalysts at the same conversion of 3.5% (Fig. 9A) and 37% (Fig. 9B), to enable a fair comparison. Clearly, both phases resulted in similar product distributions at those conversion. While oxygenates (octadecanal + octadecanol) are the main product at 3.5% conversion octadecane is the main product at 37% conversion. This indicates that the hydrodeoxygenation (HDO) pathway, although not exclusive, is dominant over both catalysts.

During HDO, stearic acid is first hydrogenated to form octadecanal. Octadecanal can be either dehydrogenated and decarbonylated to form heptadecane or hydrogenated to form octadecanol. Octadecanol is dehydrated to form octadecene, which is hydrogenated to octadecane [10–12,46]. Though HDO is the major pathway some heptadecane is formed which indicates that also decarbonylation/hydrogenation and/or decarboxylation (DCO) plays a small role as shown before [11,12]. Fig. 10 illustrates the reaction pathways in stearic acid deoxygenation. The predominant pathway over the Mo carbides (HDO) is indicated by red arrows.

Since we found similar TOF values and selectivities for α-MoC$_{1-x}$/CNF and β-Mo$_2$C/CNF in the stearic acid HDO, we concluded that the same catalytic sites were involved in this reaction. However, α-MoC$_{1-x}$/CNF provided faster hydrodeoxygenation (on a weight basis) than β-Mo$_2$C/CNF, which may be attributed to either carbide particle size or active site density. However, we showed before [12] by comparing β-Mo$_2$C/CNF with small (2 nm) and large carbide particles (11 nm) that the smaller particles were less active. In contrast, here, the catalyst with the smaller particle size (α-MoC$_{1-x}$/CNF) is more active than the catalyst with larger particle size (β-Mo$_2$C/CNF). Therefore, we attribute the difference in activity to difference in the crystal phase of the carbide. To gain some insight in the influence of site density on HDO, we calculated (Table 3) the site density for α-MoC$_{1-x}$/CNF and β-Mo$_2$C/CNF based on
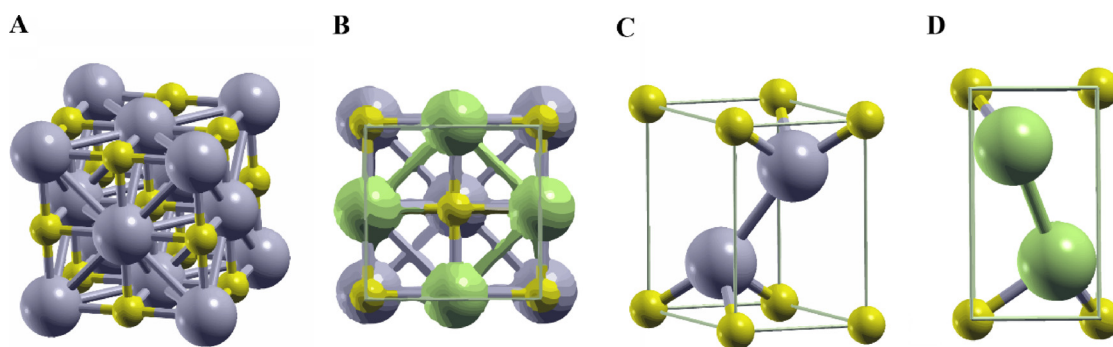

Fig. 11. A) Unit cell of fcc structure; B) Atomic configuration for (001) plane of fcc structure; C) Unit cell of hcp structure and D) Atomic configuration for (100) plane of hcp structure. Blue atoms are Mo, yellow atoms are C and green atoms are exposed Mo. (For interpretation of the references to colour in this figure legend, the reader is referred to the web version of this article.)

their crystallographic structures. Fig. 11 shows the unit cells and the atom configuration of specific planes for the face-centered cubic (fcc) and hexagonal close-packed (hcp) molybdenum carbide structures.

Table 3 contains the lattice parameters (a, b and c) and site densities for cubic α-MoC$_{1-x}$ and hexagonal β-Mo$_2$C based on literature data [47]. The α-MoC$_{1-x}$ catalyst has a site density of 0.1096 Mo atoms Å^{-2} and β-Mo$_2$C has a site density of 0.1402 Mo atoms Å^{-2}. Although higher site density is usually linked to better catalytic performance for several reactions [17,48], we observed that the catalyst with the lowest site density (α-MoC$_{1-x}$/CNF) provided faster hydrodeoxygenation (on a weight basis) than the catalyst with the higher site density (β-Mo$_2$C/CNF). We suggest that the lower site density of α-MoC$_{1-x}$/CNF resulted in more space around the Mo atoms in the α-MoC$_{1-x}$ phase, making the Mo atoms more accessible for the large reactant molecule in our experiments (stearic acid).

4. Conclusions

In our experiments, we first created 7.5 wt% molybdenum carbide catalysts on carbon nanofiber supports. Carbothermal reduction synthesis in an inert atmosphere resulted in hexagonal β-Mo$_2$C/CNF, while TPR synthesis in a 20% CH$_4$/H$_2$ atmosphere yielded cubic α-MoC$_{1-x}$/CNF. When we increased Mo loading from 7.5 to 20 wt% and performed TPR in the same CH$_4$/H$_2$ atmosphere, hexagonal β-Mo$_2$C/CNF formed. We conclude that the proportion of carbon/molybdenum available during synthesis appears to influence which crystalline phase forms.

Furthermore, although both catalysts displayed similar intrinsic activities (a TOF of 3 s^{-1} and 1 s^{-1} for α-MoC$_{1-x}$/CNF and β-Mo$_2$C/CNF, respectively), the 7.5 wt% α-MoC$_{1-x}$/CNF catalyst had a better weight-based catalytic performance than 7.5 wt% β-Mo$_2$C/CNF. We attribute this difference in catalytic performance to the difference in the crystal structure and suggest that the lower site density makes the Mo atoms more accessible for large reactant molecules.

To confirm this hypothesis, further experiments should be performed applying reactants with different carbon chain size (e.g. C3 to C20 carboxylic acids) and using 7.5 wt% α-MoC$_{1-x}$/CNF and 7.5 wt% β-Mo$_2$C/CNF as catalysts. In that way, we will be able to identify the role of site density in reactions with small and large reactant molecules.

Acknowledgements

Appendix A. Supplementary data

Supplementary material related to this article can be found, in the online version, at doi:https://doi.org/10.1016/j.apcatb.2018.09.020.

References

[1] S.T. Oyama, G. Ertl, H. Knözinger, F. Schüth, J. Weitkamp (Eds.), Handbook of Heterogeneous Catalysis, Wiley-VCH, Weinheim, 2008342–256.
[2] R.B. Levy, M. Boudart, Science 181 (1973) 547–549.
[3] S.T. Oyama, Catal. Today 15 (1992) 179–200.
[4] Z. Lin, W. Wan, S. Yao, J.G. Chen, Appl. Catal. B 233 (2018) 160–166.
[5] M. Grilc, G. Veryasov, B. Likozar, A. Jesih, J. Levec, Appl. Catal. B 163 (2015) 467–477.
[6] K. Xiong, W.-S. Lee, A. Bhan, J.G. Chen, ChemSusChem 7 (2014) 2146–2151.
[7] Y.-B. Huang, M.-Y. Chen, L. Yan, Q.-X. Guo, Y. Fu, ChemSusChem 7 (2014) 1068–1070.
[8] H. Ren, W. Yu, M. Salciccioli, Y. Chen, Y. Huang, K. Xiong, D.G. Vlachos, J.G. Chen, ChemSusChem 6 (2013) 798–801.
[9] J.A. Schaidle, J. Blackburn, C.A. Farberow, C. Nash, K.X. Steirer, J. Clark, D.J. Robichaud, D.A. Ruddy, ACS Catal. 6 (2016) 1181–1197.
[10] L.A. Sousa, J.L. Zotin, V. Teixeira da Silva, Appl. Catal. A Gen. 449 (2012) 105–111.
[11] R.W. Gosselink, D.R. Stellwagen, J.H. Bitter, Angew. Chem. Int. Ed. 52 (2013) 5089–5092.
[12] D.R. Stellwagen, J.H. Bitter, Green Chem. 17 (2015) 582–593.
[13] E.F. Mai, M.A. Machado, T.E. Davies, J.A.L. Sanchez, V. Teixeira da Silva, Green Chem. 16 (2014) 4092–4097.
[14] B. Dhandapani, T.St. Clair, S.T. Oyama, Appl. Catal. A Gen. 168 (1998) 219–228.
[15] C. Li, M. Zheng, A. Wang, T. Zhang, Energy Environ. Sci. 5 (2012) 6383–6390.
[16] J.B. Claridge, A.P.E. York, A.J. Brungs, C.M. Alvarez, J. Sloan, S.C. Tsang, M.L.H. Green, J. Catal. 180 (1998) 85–100.
[17] J.-S. Choi, G. Bugli, G.D. Mariadassou, J. Catal. 193 (2000) 238–247.
[18] T.-cun Xiao, A.P.E. York, V.C. Williams, H.A. Megren, A. Hanif, X.-ya Zhou, M.L.H. Green, Chem. Mater. 12 (2000) 3896–3905.
[19] X. Li, D. Ma, L. Chen, X. Bao, Catal. Lett. 116 (2007) 63–69.
[20] W. Gruner, S. Stolle, K. Wetzig, Int. J. Ref. Mater. Hard Mater. 18 (2000) 137–145.
[21] A.L. Jongerius, R.W. Gosselink, J. Dijkstra, J.H. Bitter, P.C.A. Bruijnincx, B.M. Weckhuysen, ChemCatChem 5 (2013) 2964–2972.
[22] Y. Qin, L. He, J. Duan, P. Chen, H. Lou, X. Zheng, H. Hong, ChemCatChem 6 (2014) 2698–2705.
[23] E. Puello-Polo, J.L. Brito, J. Mol. Catal. A Chem. 281 (2008) 85–92.
[24] Kh.V. Manukyan, A.R. Zurnachyan, S.L. Kharatyan, R.A. Mnatsakanyan, Int. J. Self-Propag. High-Temp. Synth. 20 (2011) 1–5.
[25] C.L. Roe, K.H. Schulz, Stud. Surf. Sci. Catal. 127 (1999) 121–128.
[26] H.H. Hwu, J.G. Chen, Chem. Rev. 105 (2005) 185–212.
[27] M.M. Sullivan, A. Bhan, J. Catal. 344 (2016) 53–58.
[28] Z. Li, C. Chen, E. Zhan, N. Ta, Y. Li, W. Shen, Chem. Commun. (Camb.) 50 (2014) 4469–4471.
[29] B. Frank, K. Friedel, F. Girgsdies, X. Huang, R. Schlögl, A. Trunschke, ChemCatChem 5 (2013) 2296–2305.
[30] G. Vitale, H. Guzmán, M.L. Frauwallner, C.E. Scott, P.P. Almao, Catal. Today 250 (2015) 123–133.
[31] K.-Z. Qi, G.-C. Wang, W.-J. Zheng, Surf. Sci. 614 (2013) 53–63.
[32] A. Lofberg, A. Frennet, G. Leclercq, L. Leclercq, J.M. Giraudon, J. Catal. 189 (2000) 170–183.
[33] J. Zou, M. Xiang, B. Hou, D. Wu, Y. Sun, J. Nat. Gas Chem. 20 (2011) 271–280.
[34] J. Gao, Y. Wu, C. Jia, Z. Zhong, F. Gao, Y. Yang, B. Liu, Catal. Commun. 84 (2016) 147–150.
[35] T. Matsuda, Y. Hirata, H. Itoh, H. Sakagami, N. Takahashi, Microporous Mesoporous Mater. 42 (2001) 337–344.
[36] ICDD PDF-2 database package http://www.icdd.com/products/pdf2.htm, Accessed on DATE.
[37] C.H.L. Tempelman, E.J.M. Hensen, Appl. Catal. B 176–177 (2015) 731–739.
[38] K.O. Sebakhy, G. Vitale, A. Hassan, P. Pereira-Almao, Catal. Lett. 148 (2018) 904–923.
[39] J.H. Bitter, J. Mater. Chem. 20 (2010) 7312–7321.
[40] W.-S. Lee, A. Kumar, Z. Wang, A. Bhan, ACS Catal. 5 (2015) 4104–4114.
[41] H. Wang, S. Liu, K.J. Smith, Energy Fuels 30 (2016) 6039–6049.
[42] W.-S. Lee, Z. Wang, R.J. Wu, A. Bhan, J. Catal. 319 (2014) 44–53.
[43] T.P.St. Clair, S.T. Oyama, D.F. Cox, Surf. Sci. 468 (2000) 62–76.
[44] M. Nagai, H. Tominaga, S. Omi, Langmuir 16 (2000) 10215–10220.
[45] X.-R. Shi, J. Wang, K. Hermann, J. Phys. Chem. C 114 (2010) 13630–13641.
[46] J. Han, J. Duan, P. Chen, H. Lou, X. Zheng, Adv. Synth. Catal. 353 (2011) 2577–2583.
[47] J.R. dos S. Politi, F. Viñes, J.A. Rodriguez, F. Illas, Phys. Chem. Chem. Phys. 15 (2013) 12617–12625.
[48] K.R. McCrea, J.W. Logan, T.L. Tarbuck, J.L. Heiser, M.E. Bussel, J. Catal. 171 (1997) 255–267.